JGR Space Physics

RESEARCH ARTICLE
10.1029/2021JA029253

Sensitivity of Upper Atmosphere to Different Characteristics of Flow Bursts in the Auroral Zone

Cheng Sheng[1], Yue Deng[1], Christine Gabrielse[2], Larry R. Lyons[3], Yukitoshi Nishimura[4], Roderick A. Heelis[5], and Yun-Ju Chen[5]

[1]Department of Physics, University of Texas at Arlington, Arlington, TX, USA, [2]The Aerospace Corporation, El Segundo, CA, USA, [3]Department of Atmospheric and Oceanic Sciences, University of California Los Angeles, Los Angeles, CA, USA, [4]Center for Space Physics and Department of Electrical and Computer Engineering, Boston University, Boston, MA, USA, [5]Department of Physics, University of Texas at Dallas, Richardson, TX, USA

Abstract Meso-scale plasma convection and particle precipitation could be significant momentum and energy sources for the ionosphere-thermosphere (I-T) system. Following our previous work on the I-T response to a typical midnight flow burst, flow bursts with different characteristics (lifetime, size, and speed) have been examined systematically with Global Ionosphere-Thermosphere Model (GITM) simulations in this study. Differences between simulations with and without additional flow bursts are used to illustrate the impact of flow bursts on the I-T system. The neutral density perturbation due to a flow burst increases with the lifetime, size, and flow speed of the flow burst. It was found that the neutral density perturbation is most sensitive to the size of a flow burst, increasing from ~0.3% to ~1.3% when the size changes from 80 to 200 km. A westward-eastward asymmetry has been identified in neutral density, wind, and temperature perturbations, which may be due to the changing of the forcing location in geographic coordinates and the asymmetrical background state of the I-T system. In addition to midnight flow bursts, simulations with flow bursts centered at noon, dawn, and dusk have also been carried out. A flow burst centered at noon (12.0 Local Time [LT], 73°N) produces the weakest perturbation, and a flow burst centered at dusk (18.0 LT, 71°N) produces the strongest. Single-cell and two-cell flow bursts induce very similar neutral density perturbation patterns.

Key Points:

- Neutral density perturbations due to a midnight flow burst are most sensitive to scale size
- Neutral density perturbation magnitudes due to flow bursts at different local times depend on the background state
- Single-cell and two-cell flow bursts induce similar perturbation patterns

Correspondence to:
Y. Deng,
yuedeng@uta.edu

Citation:
Sheng, C., Deng, Y., Gabrielse, C., Lyons, L. R., Nishimura, Y., Heelis, R. A., & Chen, Y.-J. (2021). Sensitivity of upper atmosphere to different characteristics of flow bursts in the auroral zone. *Journal of Geophysical Research: Space Physics*, *126*, e2021JA029253. https://doi.org/10.1029/2021JA029253

Received 16 FEB 2021
Accepted 19 SEP 2021

1. Introduction

The high-latitude ionospheric plasma convection, which is usually described as a large-scale two-cell convection pattern under southward interplanetary magnetic field (IMF) conditions and displays variations to different IMF conditions, is a manifestation of the magnetospheric dynamics driven by solar wind forcing. Besides the large-scale pattern, mesoscale ionospheric plasma flows with a horizontal scale size of 100–500 km have been identified in different observations (e.g., Chen & Heelis, 2018; Gabrielse et al., 2018, 2019). Early studies of transient and localized ionospheric plasma flows mainly focused on their correlation with nightside auroral features, such as poleward boundary intensifications (PBIs) and auroral streamers (Gallardo-Lacourt et al., 2014; Sergeev et al., 2004; Shi et al., 2012), and their possible connection with earthward bursty bulk flows (BBFs) in the plasma sheet (Pitkänen et al., 2011). For example, Shi et al. (2012) investigated the two-dimensional spatial correlation between ionospheric flows and auroral streamers and their mutual temporal evolution by overlaying the ionospheric flow measurements from the Super Dual Auroral Radar Network (SuperDARN) with the concurrent global-scale auroral images from the Wideband Imaging Camera (WIC) on board the Imager for Magnetopause-to-Aurora Global Exploration (IMAGE) satellite. Their results confirmed that double vortex-like flow structure is associated with auroral streamers, which had been predicted by different numerical simulations. Using a similar approach, Gallardo-Lacourt et al. (2014) examined the properties of mesoscale ionospheric flows related to auroral streamers by overlaying SuperDARN measurements with the Time History of Events and Macroscale Interactions during Substorms (THEMIS) ground-based all-sky imager (ASI) measurements. A total of 135 auroral streamers have been identified in their study, and all of them are correlated with ionospheric fast flows.

From the ionosphere-thermosphere (I-T) perspective, mesoscale ionospheric plasma flows and particle precipitation could be substantial momentum and energy sources (Carlson et al., 2012; Deng et al., 2013; Huang et al., 2014; Sheng et al., 2015). However, empirical models of ionospheric convection and particle

precipitation (e.g., Fuller-Rowell & Evans, 1987; Weimer, 2005), which mostly capture large-scale features and do not include mesoscale forcing, are usually used to drive general circulation models (GCMs). Accurate descriptions of the mesoscale forcing are in high demand to better quantify their impacts on the I-T system. Based on the 9-year SuperDARN line-of-sight ion drift velocity data from the stations at Rankin Inlet and Saskatoon, Gabrielse et al. (2018) determined typical flow widths, speeds, orientations, durations, and occurrence rates of mesoscale ionospheric plasma flows, and the dependency of these characteristics on magnetic local time, IMF clock angle, season, substorm activity, and solar cycle. They reported that typical mesoscale equatorward ionospheric plasma flows in the polar cap appear to have a characteristic width of 180 km with a median flow duration of 5 min. In the auroral zone, the typical width and duration are 140–150 km and 4 min, respectively. Meanwhile, properties of mesoscale ionospheric plasma flows have been examined using Defense Meteorological Satellite Program (DMSP) satellite measurements (Chen & Heelis, 2018, 2019a, 2019b). By analyzing ion drift measurements from the DMSP F17 during the summer months in 2012, Chen and Heelis (2018) found that the location and occurrence frequency of mesoscale ionospheric plasma flows are highly dependent on IMF conditions. Their results show that there are more flow perturbations embedded in sunward than antisunward background large-scale flow during southward IMF conditions. They further investigated the temporal characteristics of mesoscale ionospheric plasma flows by examining two consecutive DMSP satellites that have about the same orbital plane with the difference of sampling time between a few seconds and 20 min during the local summer seasons in 2007–2015 (Chen & Heelis, 2019b). The temporal characteristics are described by the rise and saturation times for growth and decay, with the rise times being shorter for small spatial scales (1–2 min, 100–200 km) and longer for large spatial scales (3–5 min, 200–400 km), the saturation time for growth being about 5–10 min for both scale sizes, and the saturation time for decay being ∼10 min for small scales and ∼20 min for large scales.

Following Chen and Heelis (2018) and Gabrielse et al. (2018), Deng et al. (2019) simulated the direct impact of mesoscale ionospheric flow bursts on the I-T system for the first time using the Global Ionosphere-Thermosphere Model (GITM). Their simulation results revealed that a single flow burst at midnight with an equatorward flow speed of ∼900 m/s over a spatial extent of 100 km in longitude and 400 km in latitude could cause the neutral density and the horizontal neutral wind speed at 300 km altitude to increase by 5% and 30 m/s, respectively. The specifications of mesoscale flow bursts in their study adopted values close to the upper limits in Chen and Heelis (2018) and Gabrielse et al. (2018). While Deng et al. (2019) demonstrated the importance of mesoscale flow bursts on the I-T system, a systematic study regarding the sensitivity of I-T response to different parameters of flow bursts is lacking. In this study, the major objective is to examine the impact of mesoscale flow bursts in the auroral zone with different properties on the I-T system.

2. Methodology

GITM is a three-dimensional global model of the coupled I-T system (Ridley et al., 2006) in a spherical coordinate system. It solves the continuity, momentum, and energy equations for the neutrals and ions self-consistently in an altitude-based grid. The model can output neutral density, composition, winds, and temperature as well as ion density, velocity, and temperature. The model does not assume a hydrostatic equilibrium in the vertical direction, which enables investigations of non-hydrostatic effects in the upper atmosphere (Deng & Ridley, 2014; Deng et al., 2008, 2011). The number of grid points in each direction can be specified and therefore the resolution is quite flexible. In this study, the model is run with a resolution of 0.5° in latitude, 0.5° in longitude, and 1/3 scale height in the vertical direction (∼1.5 km at an altitude of 100 and ∼15.0 km at an altitude of 300 km).

Weimer (2005) and Fuller-Rowell and Evans (1987) empirical models are used to specify the high-latitude electric potential and particle precipitation in GITM, respectively. Figure 1a shows the potential pattern from the Weimer (2005) model in color with the background geomagnetic conditions of $(B_x, B_y, B_z) = (0, 0, -2$ nT) and solar wind speed $V_x = -400$ km/s. Vectors on top of the potential represent the horizontal ion drifts at 350 km altitude. Figure 1b shows the electron energy flux map from the Fuller-Rowell and Evans (1987) model with the input of hemispheric power (HP) being 20 GW. All flow burst simulations in this study are conducted under winter solstice condition with F10.7 = 150 sfu. A similar approach as in Deng et al. (2019) has been adopted in this study to introduce additional flow bursts in GITM simulations. A flow burst is implemented by adding a mini two-cell potential pattern (a negative cell and a positive cell) on top

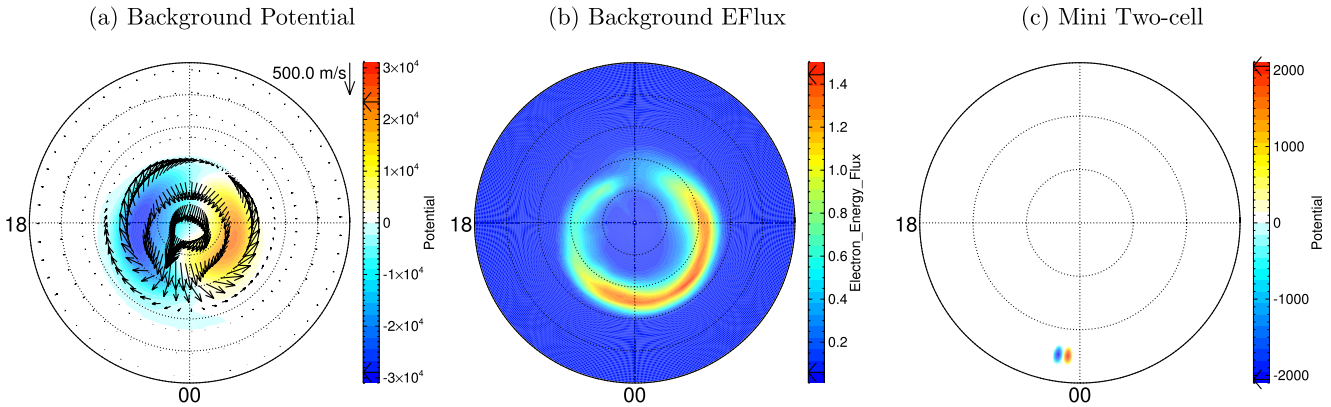

Figure 1. (a) Background electric potential (V) in color and horizontal plasma flows as vectors, (b) Background electron precipitation energy flux (mW/m^2), and (c) A mini two-cell potential (V) pattern corresponding to a flow burst centered at (23.5 LT, 65°N). In each plot, the circles denote the latitude every 10°. In panels (a) and (b), the most outside ring is 40°N, and in panel (c), the most outside ring is 60°N. Arrows in the color bar mark the maximum and minimum values of the contour.

of the background Weimer (2005) potential. Figure 1c shows an example of a mini two-cell potential pattern centered at (23.5 LT, 65°N), which corresponds to a flow burst with an equatorward major flow at the center and poleward returning flows on the two sides. The potential of the positive cell peaks at its center, and two Gaussian distributions in the zonal and meridional directions are used to specify the potential off the center. The negative cell mirrors the positive cell, and therefore the maximum potential of the positive and negative cells is equal to half of the total potential drop. The potential approaches zero near the boundary of the mini two-cell pattern so that the mini two-cell potential smoothly merges with the background potential. For a midnight flow burst as shown in Figure 1c, the negative cell is located westward of the positive cell so that the major flow is roughly in the same direction as the background flow determined by the Weimer (2005) potential pattern. In this paper and also in Deng et al. (2019), the size of the major flow inside the flow burst is half of its total size, that is, the width of each returning flow on the two sides of the major flow is half of the width of the major flow. In addition, the mini two-cell pattern has been set up so that it has a similar extent in the zonal and meridional directions. Table 1 lists the three major characteristics used to describe a flow burst, that is, "Lifetime," "Size," and "Speed." "Lifetime" represents how long the flow burst forcing is turned on in our simulation. "Size" represents the width of the major flow in the direction perpendicular to the flow. "Speed" represents the maximum speed of the major flow at F-region altitudes, where $E \times B$ drifts dominate the ion motion. "Speed" is an indication of the potential drop if "Size" is given, but "Speed," instead of a potential drop, is used as it is more convenient to align with measurements. The background particle precipitation is doubled over the major flow to account for the enhancement of precipitation associated with ionospheric flow bursts. The increase in particle precipitation reflects the expected and observed presence of large gradients in precipitation flux. Here we have not attempted to partition the contributions of precipitation and enhanced frictional heating, but rather to examine their combined effects as a function of spatial scale and location. In this study and also in Deng et al. (2019) the flow burst forcing is assumed to be constant during its lifetime.

Table 1
According to the Characteristics of Flow Bursts Shown in Chen and Heelis (2018) and Gabrielse et al. (2018), Low, Median, and High Values Are Selected for Lifetime, Size, and Speed

	Lifetime (min)	Size (km)	Speed (m/s)
Low value	2	80	140
Median value	5	140	400
High value	10	200	700
Location	Midnight/dayside/dawn/dusk		
No. of cells	Two cells/single cell		

Note. Meanwhile, flow bursts at four different locations (midnight, noon, dawn, and dusk) and under two different configurations (two-cell and single-cell) have also been compared. With a simulation resolution of 0.5° in latitude and 0.5° in longitude, there are 2 and 6 grid points in the meridional and zonal directions to resolve the smallest flow burst listed in the table when the flow burst is centered at (23.5 LT, 65°N).

3. Results

3.1. Midnight Flow Bursts With Different Characteristics

In Deng et al. (2019), the impact of flow bursts, whose spatial size and temporal duration are close to the upper limits as derived from observations, has been examined through GITM simulations. However, it is not clear how sensitive the I-T system is to different characteristics of ionospheric flow bursts. Based on the results reported in Chen and Heelis (2018) and Gabrielse et al. (2018), the low, median, and high values

have been determined for the three major characteristics ("Lifetime," "Size," and "Speed") used to describe an ionospheric flow burst, as shown in Table 1. For example, a short, median, and long lifetime of an ionospheric flow burst is defined as 2, 5, and 10 min, respectively. To evaluate the sensitivity of the I-T system to the lifetime of ionospheric flow bursts, four different GITM simulations have been conducted including a background run (purely driven by Weimer [2005]) and three perturbed runs. In the perturbed runs, the flow burst forcing is turned on at the beginning of the simulation ($T = 0$ min), and is turned off at 2-min simulation time ($T = 2$ min) for the short lifetime case, at $T = 5$ min for the median lifetime case, and at $T = 10$ min for the long lifetime case. All the three flow bursts are centered at (23.5 LT, 65°N) and the high values are used for the other two characteristics, that is, "Size" = 200 km and "Speed" = 700 m/s. Neutral density measurements, mostly from low-Earth orbit (LEO) satellites, are more abundant than neutral temperature and wind measurements in recent years, so we have decided to focus on neutral density perturbations in this study. Neutral density perturbation (percentage difference in neutral density between a perturbed run and the background run) at 405 km altitude is examined and the perturbation magnitudes due to different lifetimes are compared. Similar analysis has also been performed for different sizes and different speeds.

When the flow burst forcing is turned on and off, dynamic ionospheric and thermospheric disturbances can be identified at and near the source region. About 15 min after the forcing is turned off, the perturbations are more related to the traveling atmospheric disturbances (TADs) and traveling ionospheric disturbances (TIDs) propagating away from the source region (Deng et al., 2019) and therefore can be identified in a relatively large area. In this study, our main focus is the perturbations related to TADs. Figure 2 presents the neutral density perturbation at 405 km altitude and at $T = 30$ min for different lifetimes (top row), different sizes (middle row), and different speeds (bottom row). Figures 2c, 2f and 2i show the neutral density perturbation due to a midnight flow burst with a lifetime of 10 min, a width of 200 km for the major flow, and a maximum speed of 700 m/s. Those three figures are identical and the duplication is to help with the comparison in each row. The neutral density perturbation propagates radially outward from the source region, and the signals of TADs can be easily identified in each plot. Similar TAD signals can also be identified in the neutral temperature and wind perturbations. As shown in Figure 2, neutral density perturbation magnitude increases with lifetime, size, and plasma speed. For example, the maximum neutral density perturbation at 405 km changes from ~0.6% for a 2-min flow burst, to ~1.4% for a 5-min flow burst, and to ~2.0% for a 10-min flow burst (cf. first row in Figure 2). Perturbations propagating westward are usually larger than those propagating eastward, and this westward-eastward asymmetry has also been identified in Deng et al. (2019). Interestingly, a comparison of Figures 2b, 2e and 2h in the middle column indicates that there is a tradeoff among those three variables. The neutral density perturbation caused by a flow burst with a moderate lifetime, but a large size and a high plasma speed (Figure 2b) is comparable to that caused by a flow burst with a longer lifetime, but a smaller size (Figure 2e), or a flow burst with a longer lifetime, but a lower speed (Figure 2h). This indicates that all these three parameters are important for the thermospheric perturbation and the combination of them decides the total energy inputs and the net effects on the upper atmosphere.

While Figure 2 presents some snapshots of the neutral density perturbation at 405 km, it does not include the temporal variation of the perturbation. The neutral density perturbation at 405 km altitude and at the location 500 km west of the center of the flow burst (23.5 LT, 65°N) from $T = 0$ min to $T = 60$ min is plotted in Figure 3. This location has been chosen since (a) it is away from the source region and the perturbation at this location more or less represents the TAD effect, and (b) the perturbation in the westward direction is larger compared to the perturbation in other directions as mentioned in the previous paragraph. In Figure 3a, the blue, red, and magenta solid lines depict the neutral density perturbations due to a midnight flow burst with lifetimes of 2, 5, and 10 min, respectively. The size and the plasma speed are kept as 200 km and 700 m/s for Figure 3a. After the flow burst forcing is turned off (marked by the vertical dashed lines), it roughly takes about 10 min for the neutral density perturbation to reach its maximum. The maximum neutral density perturbation is ~0.5%, ~1.0%, and ~1.3% for a 2-, 5-, and 10-min flow burst, respectively. Figures 3b and 3c are the same as Figure 3a except for different sizes and different speeds, respectively. Figure 3b shows the comparison for different sizes when the lifetime and the speed are kept as 10 min and 700 m/s. Figure 3c shows the comparison for different plasma speeds when the lifetime and the size are kept as 10 min and 200 km. The magnitude of the maximum neutral density perturbation and its sensitivity to lifetime, size, and speed are generally comparable. The maximum value of each line in Figure 3 is plotted in

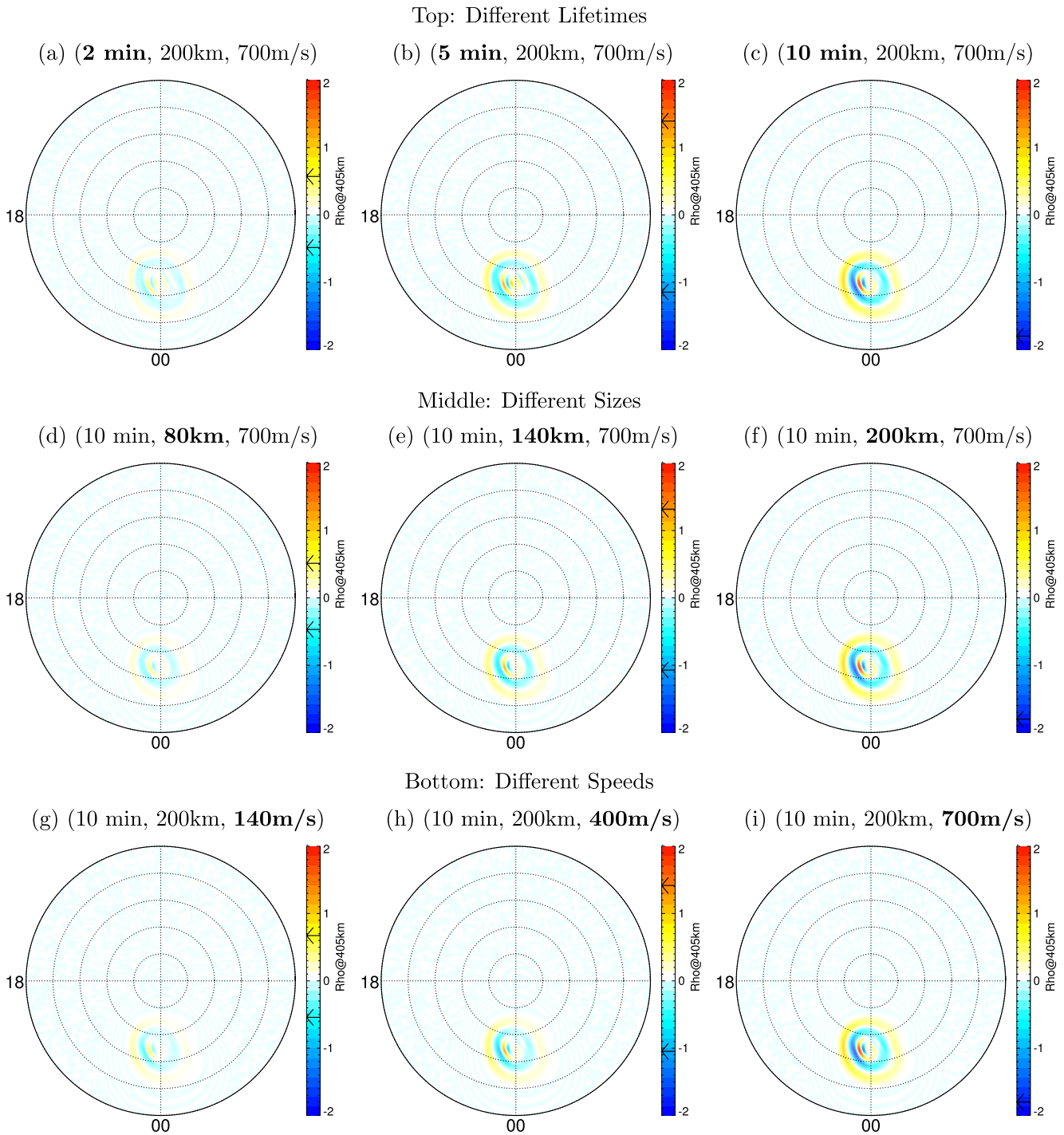

Figure 2. Neutral density perturbations (%) at 405 km and at 30-min simulation time due to flow bursts with different characteristics (top row for different lifetimes, middle row for different sizes, and bottom row for different speeds). Panels (c), (f), and (i) are identical and the purpose of duplication is to help the comparison in each row. In each plot, the circles denote the latitude every 10°, and the most outside ring is 40°N. Arrows in the color bar mark the maximum and minimum of the contour in color.

Figure 4 to better illustrate the trend of the maximum neutral density perturbation. In general, the trends for the three variables are comparable, but the I-T system is more sensitive to the size of ionospheric flow bursts than to the other two, as the maximum neutral density perturbation varies the most (from ~0.3% to ~1.3%) when the size changes from the low value to the high value. The neutral density perturbation magnitude due

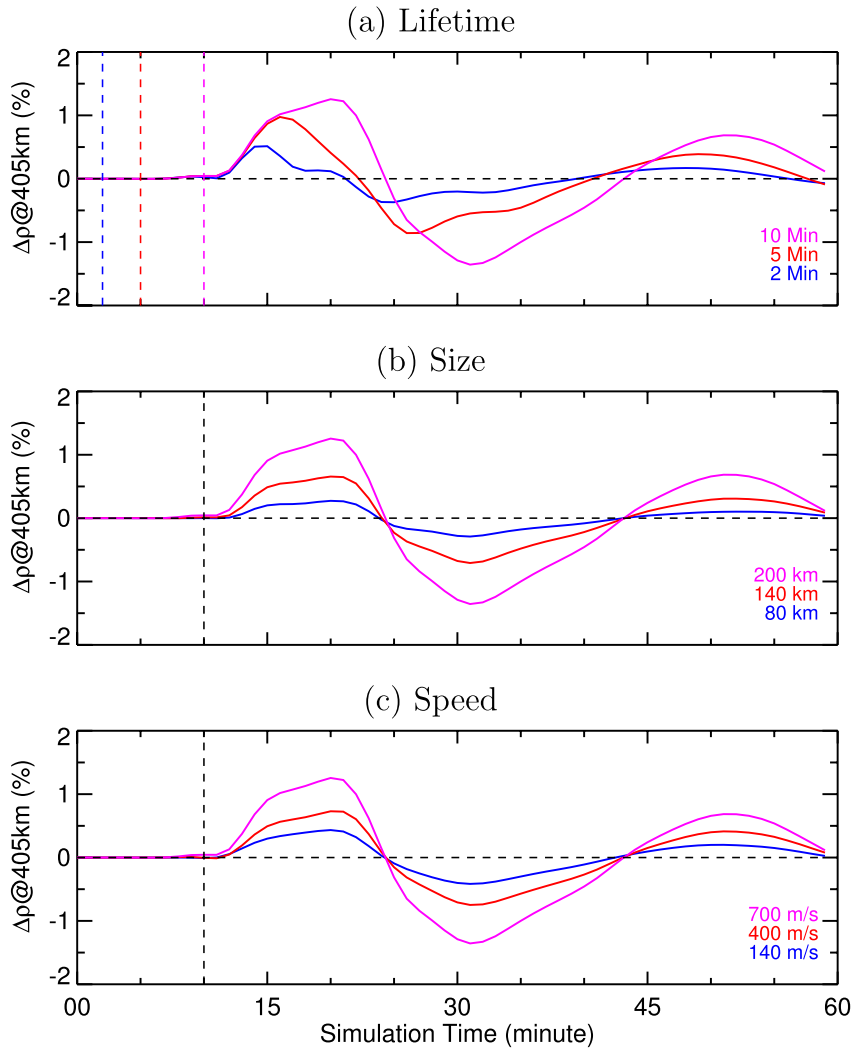

Figure 3. Neutral density perturbation at 405 km altitude and at the location 500 km west of the center of flow burst (23.5 LT, 65°N) with different lifetimes (top), different sizes (middle), and different speeds (bottom). The vertical dashed lines mark the timing when the flow burst forcing is turned off.

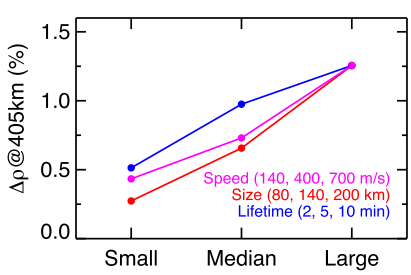

Figure 4. Maximum neutral density perturbations at 405 km altitude and at the location 500 km west of the center of flow burst, that is, maxima of the nine lines in Figure 3. Different colors represent the variations of the maximum perturbations due to different flow burst characteristics, such as lifetime (magenta), speeds (red), and sizes (blue).

to a single ionospheric flow burst is relatively small compared to the typical amplitude of large-scale traveling atmospheric disturbances (LSTADs) derived from satellite neutral density measurements (e.g., Bruinsma & Forbes, 2008, 2010). However, the size of flow bursts is much smaller than the area of large geomagnetic energy inputs during storm periods, which causes LSTADs. The total energy input accompanying a flow burst is less than 1 GW, and the total Joule heating at high latitudes can easily be more than 100 GW during a moderate storm. Taking into account the difference in the size and total energy inputs, it is reasonable to have a much smaller neutral density perturbation caused by a localized flow burst. Meanwhile, the scale of the TADs due to ionospheric flow bursts is more or less a mesoscale TAD, which is smaller than the typical scale of LSTADs (>1,000 km). These localized flow bursts thus add mesoscale structures to the storm-time ionospheric and thermospheric disturbances.

As mentioned above, the response of the I-T system to midnight flow bursts displays a westward-eastward asymmetry such that the perturba-

tions in the westward direction are larger than those in the eastward direction. In Deng et al. (2019), it was proposed that the Coriolis force might contribute to the asymmetry. Test runs (results not shown) have been performed with the Coriolis force being turned off in GITM, and its impact on the westward-eastward asymmetry has been found to be minor. Instead, it may be related to the forcing being fixed with respect to local time. By keeping the flow burst forcing at a fixed local time and latitude, the geographic location (Longitude, Latitude) of the forcing is changing with time as the Earth rotates. Therefore, gravity waves may be triggered at different geographic locations and interactions between these waves are expected. To demonstrate the impact of the changing forcing location on the westward-eastward asymmetry, an additional run, in which the flow burst forcing (10 min, 200 km, 700 m/s) is centered at a fixed longitude and a fixed latitude (172.5°E, 65°N) instead of a fixed local time and a fixed latitude, has been conducted. The simulation starts at 12:00 UT, when the corresponding longitude for 23.5 LT is 172.5°E. Figure 5 shows the neutral density (top row), neutral temperature (middle row), and zonal wind (bottom row) perturbations at 405 km altitude and at $T = 50$ min when a flow burst is centered at a fixed local time (23.5 LT, 65°N) (left column) and is centered at a fixed longitude (172.5°E, 65°N) (right column). The westward-eastward asymmetry is weaker when the flow burst forcing is centered at a fixed geographic location, which indicates that the interactions between the gravity waves originating from different geographic locations do play an important role in producing the westward-eastward asymmetry.

Changing of the forcing location with the Earth's rotation is certainly not the sole mechanism that causes the westward-eastward asymmetry identified in this study as well as in Deng et al. (2019) since the asymmetry still presents in the neutral perturbations due to a flow burst centered at a fixed longitude and a fixed latitude (Figures 5b, 5d and 5f). It is believed that the asymmetry in the background state of the I-T system may be another important source. The momentum equations may help to understand how the background state may contribute to the asymmetry. For example, the vertical momentum equation (Equation 14 in Ridley et al., 2006) shows that the gradient of the background neutral temperature can contribute to the pressure gradient force and the temporal variation of neutral winds, which is important for TAD propagation. However, neutral density, temperature, and neutral winds are tightly coupled through continuity, momentum, and energy equations in GCMs (Ridley et al., 2006), and it is challenging to further diagnose which parameter(s) of the background state plays the most important role.

3.2. Ionospheric Flow Bursts at Different Locations

In our previous study (Deng et al., 2019) and in Section 3.1, the main focus is the impact of ionospheric flow bursts located near midnight, as Gallardo-Lacourt et al. (2014) suggest that ionospheric flow bursts predominantly occur within 2–3 hr of midnight. However, the ion drift measurements from DMSP satellites reveal that ionospheric flow bursts can occur at different local times (Chen & Heelis, 2018, 2019a, 2019b), and how the I-T system responds to the ionospheric flow bursts at different local times becomes an interesting research question. To answer this question, another three perturbed runs have been conducted. The top row of Figure 6 shows the setup of mini two-cell potential patterns at noon (Figure 6a), dawn (Figure 6b), and dusk (Figure 6c). The centers of the two-cell patterns locate at (12.0 LT, 73°N), (6.0 LT, 68°N), and (18.0 LT, 71°N), respectively. The latitudes have been chosen so that the locations are close to the center of the auroral zone and the particle precipitation at those particular locations is strongest compared with other latitudes at the same local times (see Figure 1b). All three flow bursts have a lifetime of 10 min and a width of 200 km. The maximum speeds of the major flows at F-region altitudes are all set to be 700 m/s, but the potential drops are not identical since the magnetic fields are different at different locations. Meanwhile, the major flows are in the same directions as the background flows (see Figure 1a), and thus the relative location of the negative cell and the positive cell is different at different local times. For example, at noon and midnight, the positive cell is on the dawn side of the mesoscale configuration, but at dawn and dusk, the positive cell is on the dusk side of the mesoscale configuration.

The bottom row of Figure 6 shows the corresponding neutral density perturbation at 405 km altitude and at $T = 50$ min driven by the flow bursts shown in the top row of Figure 6. Compared with Figure 5a, the neutral density perturbation at 405 km altitude due to flow bursts at noon, dawn, and dusk shows a very similar pattern as those due to a flow burst at midnight, but with different magnitudes. The maximum perturbations due to flow bursts at midnight, noon, dawn, and dusk are ~2.0%, ~0.9%, ~1.0%, and 2.2%,

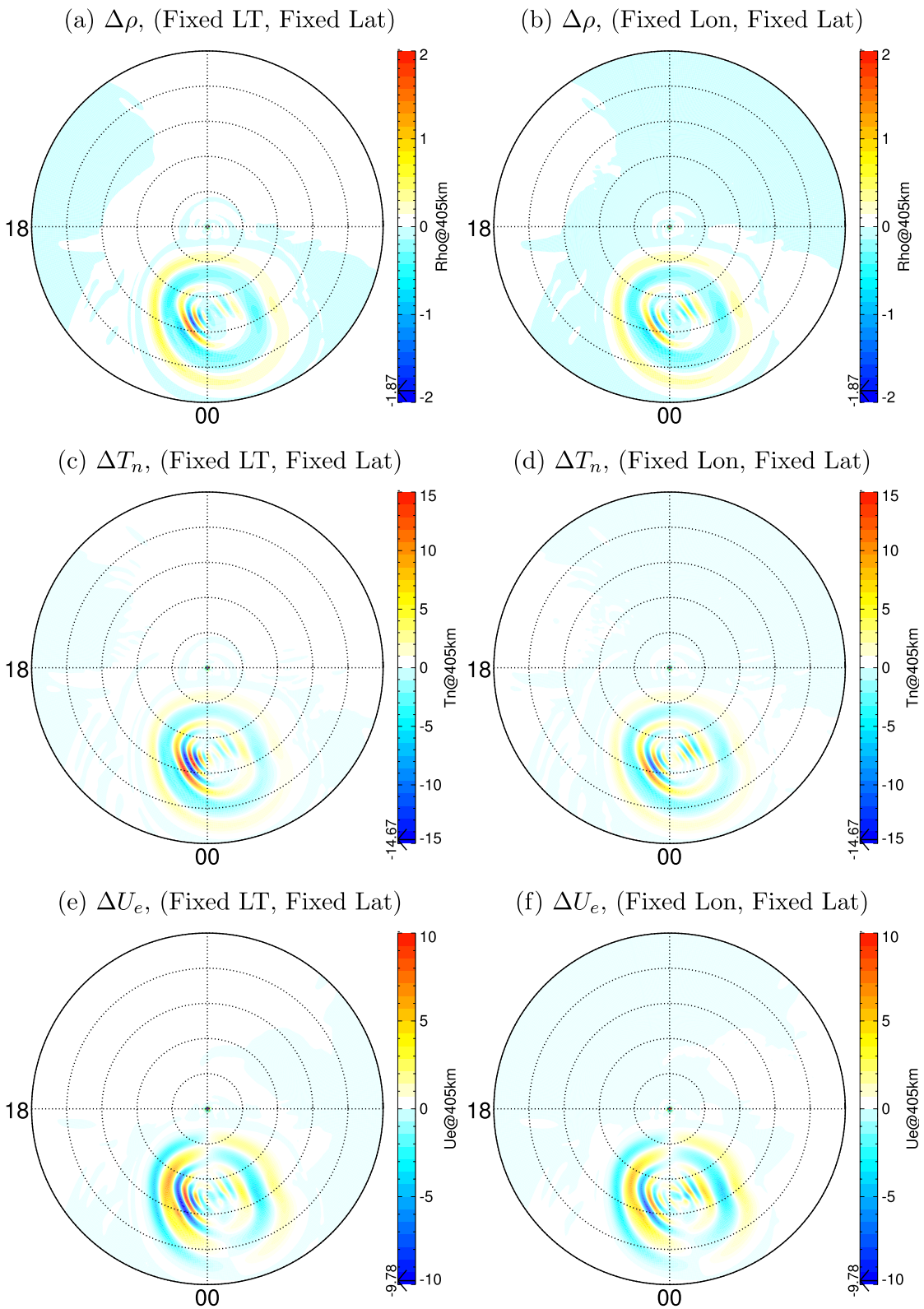

Figure 5. Neutral density (top row), neutral temperature (middle row), and zonal wind (bottom row) perturbations at 405 km altitude and at 50-min simulation time due to a flow burst centered at a fixed local time and a fixed latitude ([23.5 LT, 65°N], left column) and at a fixed longitude and a fixed latitude ([172.5°E, 65°N], right column). The westward-eastward asymmetry is relatively weaker if the forcing is centered at a fixed longitude and a fixed latitude. In each plot, the circles denote the latitude every 10°, and the most outside ring is 40°N.

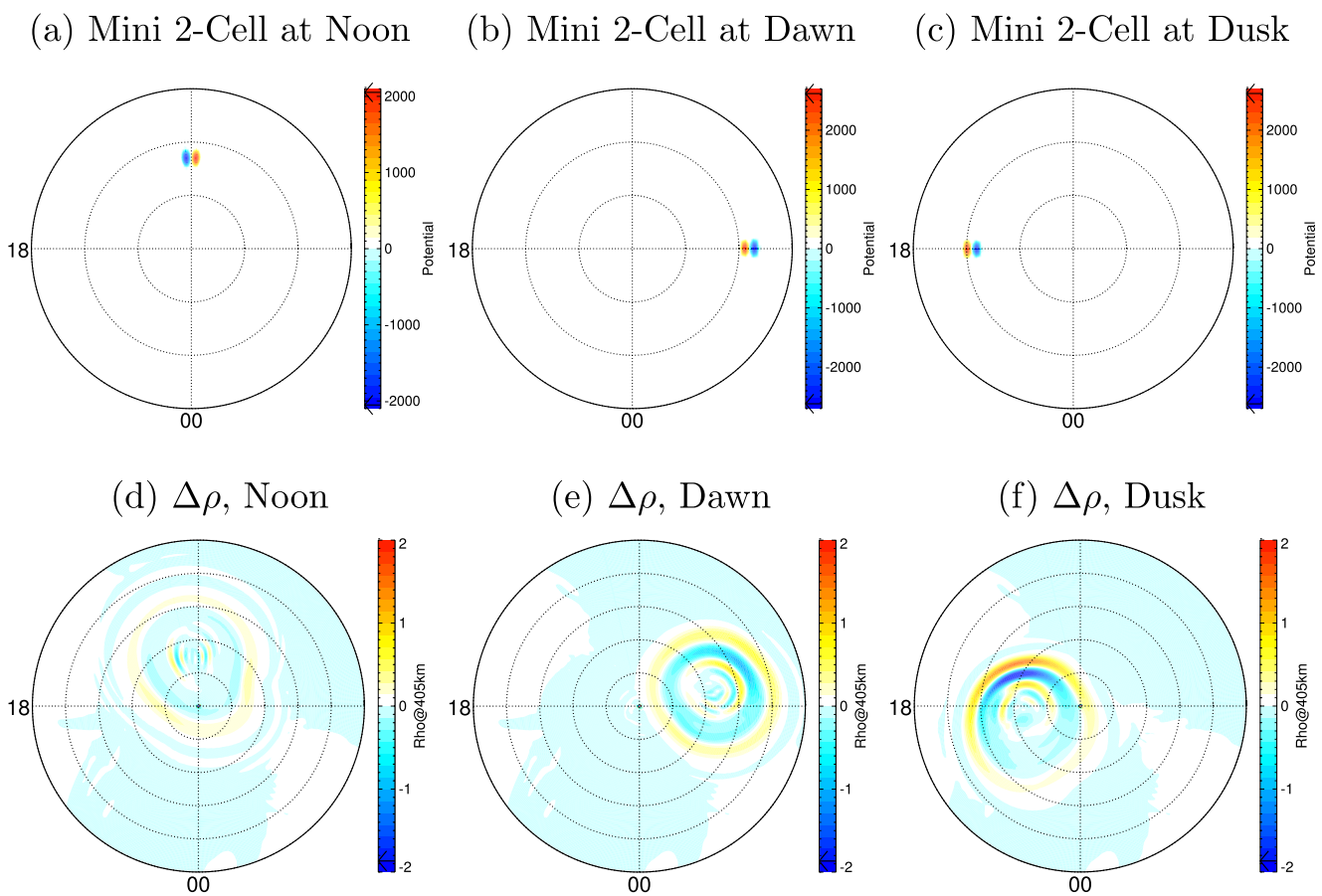

Figure 6. Top row: mini two-cell potential pattern for a flow burst centered at (a) Noon (12.0 LT, 73°N), (b) Dawn (6.0 LT, 68°N), and (c) Dusk (18.0 LT, 71°N). Bottom row: neutral density perturbations at 405 km altitude and at 50-min simulation time due to a flow burst at (d) Noon, (e) Dawn, and (f) Dusk. The plots in the bottom row can be compared with Figure 5a, which shows the neutral density perturbation due to a midnight flow burst centered at midnight (23.5 LT, 65°N). In each plot, the circles denote the latitude every 10°. In panels (a)–(c), the most outside ring is 60°N; in panels (d)–(f), the most outside ring is 40°N. Arrows in the color bar mark the maximum and minimum of the contour in color.

respectively. The flow burst centered at dusk (18.0 LT, 71°N) produces the strongest perturbation, which is more than two times larger than that at noon (12.0 LT, 73°N). There are a few sources that could contribute to the differences in the neutral density perturbations: (a) the background particle precipitation is different; (b) flow bursts at different local times are located at different latitudes; (c) even when located at the same latitudes, the background states of the I-T system are different at different local times. Further analyses are needed to fully understand the physical processes contributing to the local-time-dependent I-T response to ionospheric flow bursts, which will be an important future study.

3.3. Single-Cell Versus Two-Cell Flow Bursts

Following studies of ionospheric flow bursts using SuperDARN observations (Gallardo-Lacourt et al., 2014; Gabrielse et al., 2018), mini two-cell potential patterns have been adopted to implement flow bursts in our simulations. Meanwhile, DMSP measurements show that both single-cell and two-cell configurations exist (Chen & Heelis, 2018, 2019a, 2019b) and more single-cell perturbations are observed than two-cell configurations. The major difference between them is that a single-cell flow burst consists of a major flow with a single returning flow while a two-cell flow burst consists of a major flow with returning flows on the two sides. In this section, two additional runs, in which flow bursts are described by single-cell potential patterns, have been performed to demonstrate whether the I-T system responds differently to single-cell and two-cell flow bursts.

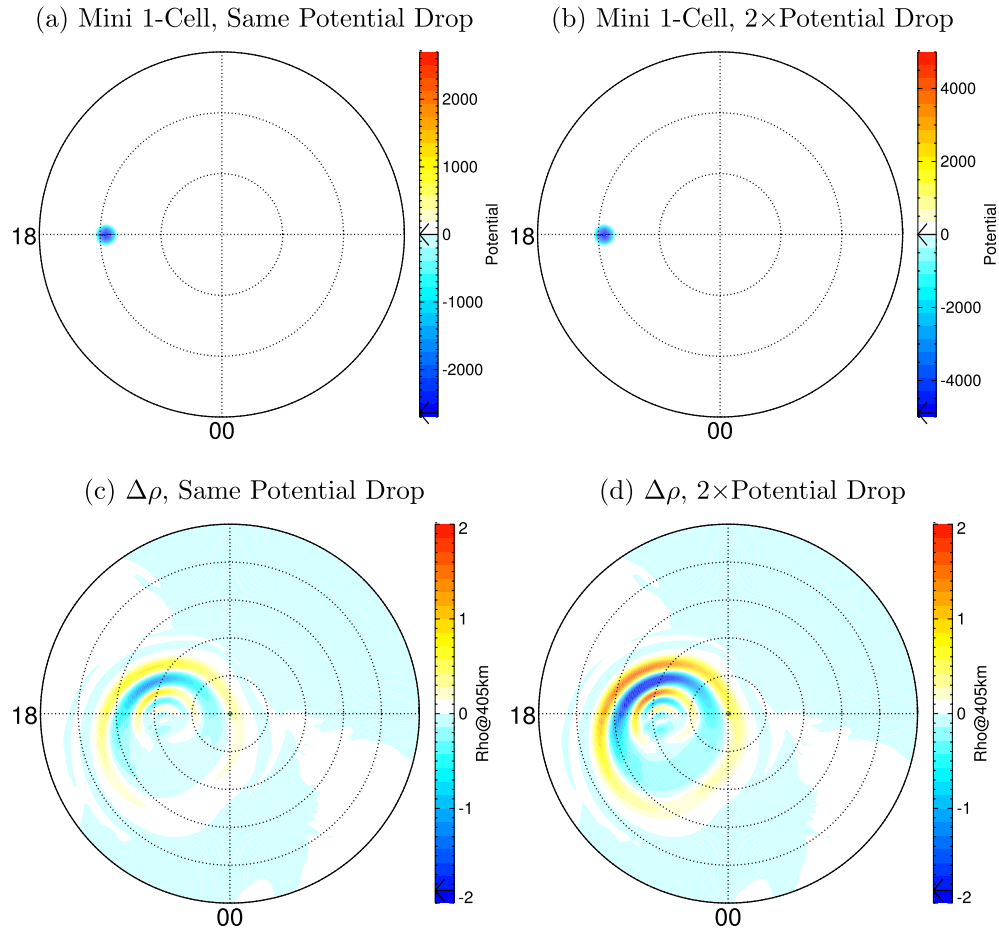

Figure 7. Top row: Potential distributions for single-cell flow bursts centered at (18LT, 71°N). Panels (a) and (b) can be compared with Figure 6c, which shows the potential distribution for a two-cell flow burst centered at the same location. In panel (a), the potential drop is kept the same as the potential drop of the negative cell in the two-cell configuration, but the size is double of the negative cell in the two-cell configuration as shown in Figure 6c. In panel (b), the potential drop is two times as that in panel (a), so the maximum flow speed is comparable to that in the two-cell configuration. The corresponding neutral density perturbations at 405 km and at 50-min simulation time are shown at the bottom row, which should be compared with Figure 6f. In each plot, the circles denote the latitude every 10°. In panels (a) and (b), the most outside ring is 60°N; in panels (c) and (d), the most outside ring is 40°N. Arrows in the color bar mark the maximum and minimum of the contour in color.

The top row of Figure 7 shows the configurations of the single-cell potential patterns in the two additional runs. Both single-cell patterns are centered at (18.0 LT, 71°N), and have the same size (400 km in both zonal and meridional directions) and the same lifetime (10 min) as the two-cell pattern in Figure 6c. In the first perturbed run (Figure 7a), the single-cell pattern can be viewed as half of the two-cell pattern, with only the negative cell and the potential drop of the single-cell configuration being the same as the negative cell in the two-cell configuration (Figure 6c). However, the size of the single-cell pattern is two times of the negative cell in the two-cell configuration. In the second perturbed run (Figure 7b), the potential drop of the single-cell pattern is doubled so that the maximum perturbation electric field or flow speed is roughly the same as the two-cell configuration (Figure 6c), since the size of the single-cell is doubled compared to one cell in the two-cell configuration. The bottom row of Figure 7 shows the corresponding neutral density perturbation at 405 km altitude and at $T = 50$ min. The neutral density perturbation shown in Figure 7d is almost two times that in Figure 7c, which is due to the enhancement of the flow speed. In terms of magnitude, Figure 7d is closer to the value shown in Figure 6f than Figure 7c, which indicates that when both the total size and the maximum flow speed (instead of the maximum potential drop) of a single-cell are comparable to those of a two-cell, the pattern and the magnitude of the neutral density perturbation due to

a single-cell flow burst are very similar to those due to a two-cell flow burst. It is therefore concluded that there is no significant difference in the TAD-related I-T response to single-cell and two-cell ionospheric flow bursts characterized by the same spatial scale and the same flow speed. However, it is anticipated that the perturbations in plasma density may not be identical when the flow burst forcing is present since single-cell and two-cell ionospheric flow bursts have different flow structures.

4. Summary

In this study, the response of neutral density at 405 km altitude to midnight flow bursts with different characteristics (lifetime, size, and speed) have been examined with GITM simulations. The differences between simulations with and without flow bursts illustrate the impact of flow bursts on the I-T system. Away from the source region, neutral density perturbations can be mostly described as TADs, and similar TAD signals can be identified in neutral temperature and wind perturbations. The neutral density perturbation increases with the flow lifetime, the size, and the flow speed of an ionospheric flow burst. To examine the sensitivity of the I-T system to different flow burst characteristics, maximum neutral density perturbations at 405 km altitude and at the location 500 km west of the center of the flow burst have been chosen as the parameter for quantification. The sensitivity to lifetime, size, and speed is generally comparable, while quantitatively the I-T system is more sensitive to the size of an ionospheric flow burst than the other two. The maximum neutral density perturbation at 405 km increases from ~0.3% to ~1.3% when the width of the major flow changes from 80 to 200 km.

A westward-eastward asymmetry has been identified in the neutral density perturbation at 405 km altitude, which may be due to both the changing of the forcing location and the asymmetry in the background state of the I-T system. Thus, the nature of the propagating disturbances depends on the motion of the mesoscale convection feature with respect to the background flow. Comparisons among the GITM simulations with flow bursts at four different local times (midnight, noon, dawn, and dusk) show that flow bursts cause a similar neutral density perturbation pattern at different local times but with different wavelengths and magnitudes, and the flow burst centered at dusk produces the strongest perturbation. Major sources contributing to the differences include: (a) the background geomagnetic forcing (both particle precipitation and ion convection) is different at different local times; (b) the geographic latitudes of the flow bursts at different local times are slightly different due to the displacement between geographic and geomagnetic coordinates; and (c) the background ionospheric and thermospheric conditions also have a strong local time dependence. Our simulation results also illustrate that single-cell and two-cell flow bursts induce similar perturbations in the neutral density when both the total size and the maximum flow speed of a single-cell are comparable to those of a two-cell.

Acknowledgments
This study at the University of Texas at Arlington was supported by NASA through grants 80NSSC20K0195 and 80NSSC20K1786, and AFOSR through awards FA9559-16-1-0364. Research by CG was supported by FA9559-16-1-0364. The study of YN was supported by NASA grant 80NSSC18K0657 and 80NSSC20K0725, NSF grant AGS-1907698, and AFOSR grant FA9559-16-1-0364. Research at UCLA and UTD was supported by AFOSR through awards FA9559-16-1-0364. The authors thank the support from the ISSI for the international team on "Multi-Scale Magnetosphere-Ionosphere-Thermosphere Interaction." The authors acknowledge the Texas Advanced Computing Center (TACC) at The University of Texas at Austin for providing HPC resources that have contributed to the research results reported within this study. URL: http://www.tacc.utexas.edu.

Data Availability Statement

The model outputs are available at https://www.doi.org/10.5281/zenodo.4543689.

References

Bruinsma, S. L., & Forbes, J. M. (2008). Medium-to large-scale density variability as observed by CHAMP. *Space Weather*, *6*(8). https://doi.org/10.1029/2008sw000411

Bruinsma, S. L., & Forbes, J. M. (2010). Large-scale traveling atmospheric disturbances (LSTADs) in the thermosphere inferred from CHAMP, GRACE, and SETA accelerometer data. *Journal of Atmospheric and Solar-Terrestrial Physics*, *72*(13), 1057–1066. https://doi.org/10.1016/j.jastp.2010.06.010

Carlson, H. C., Spain, T., Aruliah, A., Skjaeveland, A., & Moen, J. (2012). First-principles physics of cusp/polar cap thermospheric disturbances. *Geophysical Research Letters*, *39*(19). https://doi.org/10.1029/2012gl053034

Chen, Y. J., & Heelis, R. A. (2018). Mesoscale plasma convection perturbations in the high-latitude ionosphere. *Journal of Geophysical Research: Space Physics*, *123*(9), 7609–7620. https://doi.org/10.1029/2018ja025716

Chen, Y. J., & Heelis, R. A. (2019a). Spatial characteristics of mesoscale plasma flow perturbations and accompanying electron precipitation in the high-latitude ionosphere. *Journal of Geophysical Research: Space Physics*. *124*(12), 10444–10458. https://doi.org/10.1029/2019ja027166

Chen, Y. J., & Heelis, R. A. (2019b). Temporal characteristic of the mesoscale plasma flow perturbations in the high-latitude ionosphere. *Journal of Geophysical Research: Space Physics*, *124*(1), 459–469. https://doi.org/10.1029/2018ja026128

Deng, Y., Fuller-Rowell, T. J., Akmaev, R. A., & Ridley, A. J. (2011). Impact of the altitudinal Joule heating distribution on the thermosphere. *Journal of Geophysical Research: Space Physics*, *116*(A5). https://doi.org/10.1029/2010ja016019

Deng, Y., Fuller-Rowell, T. J., Ridley, A. J., Knipp, D., & Lopez, R. E. (2013). Theoretical study: Influence of different energy sources on the cusp neutral density enhancement. *Journal of Geophysical Research: Space Physics*, *118*(5), 2340–2349. https://doi.org/10.1002/jgra.50197

Deng, Y., Heelis, R., Lyons, L. R., Nishimura, Y., & Gabrielse, C. (2019). Impact of flow bursts in the auroral zone on the ionosphere and thermosphere. *Journal of Geophysical Research: Space Physics*. *124*(12), 10459–10467. https://doi.org/10.1029/2019ja026755

Deng, Y., Richmond, A. D., Ridley, A. J., & Liu, H. L. (2008). Assessment of the non-hydrostatic effect on the upper atmosphere using a general circulation model (GCM). *Geophysical Research Letters*, *35*(1). https://doi.org/10.1029/2007gl032182

Deng, Y., & Ridley, A. J. (2014). Simulation of non-hydrostatic gravity wave propagation in the upper atmosphere. *Annales Geophysicae*, *32*(4), 443–447. https://doi.org/10.5194/angeo-32-443-2014

Fuller-Rowell, T. J., & Evans, D. S. (1987). Height-integrated Pedersen and Hall conductivity patterns inferred from the TIROS-NOAA satellite data. *Journal of Geophysical Research*, *92*(A7), 7606–7618.

Gabrielse, C., Nishimura, Y., Lyons, L., Gallardo-Lacourt, B., Deng, Y., & Donovan, E. (2018). Statistical properties of mesoscale plasma flows in the nightside high-latitude ionosphere. *Journal of Geophysical Research: Space Physics*, *123*(8), 6798–6820. https://doi.org/10.1029/2018ja025440

Gabrielse, C., Pinto, V., Nishimura, Y., Lyons, L., Gallardo-Lacourt, B., & Deng, Y. (2019). Storm time mesoscale plasma flows in the nightside high-latitude ionosphere: A statistical survey of characteristics. *Geophysical Research Letters*, *46*(8), 4079–4088. https://doi.org/10.1029/2018gl081539

Gallardo-Lacourt, B., Nishimura, Y., Lyons, L. R., Zou, S., Angelopoulos, V., Donovan, E., et al. (2014). Coordinated SuperDARN THEMIS ASI observations of mesoscale flow bursts associated with auroral streamers. *Journal of Geophysical Research: Space Physics*, *119*(1), 142–150.

Huang, C. Y., Su, Y. J., Sutton, E. K., Weimer, D. R., & Davidson, R. L. (2014). Energy coupling during the August 2011 magnetic storm. *Journal of Geophysical Research: Space Physics*, *119*(2), 1219–1232. https://doi.org/10.1002/2013ja019297

Pitkänen, T., Aikio, A. T., Amm, O., Kauristie, K., Nilsson, H., & Kaila, K. U. (2011). EISCAT-Cluster observations of quiet-time near-Earth magnetotail fast flows and their signatures in the ionosphere. *Annales Geophysicae*, *29*(2). https://doi.org/10.5194/angeo-29-299-2011

Ridley, A. J., Deng, Y., & Toth, G. (2006). The global ionosphere-thermosphere model. *Journal of Atmospheric and Solar-Terrestrial Physics*, *68*(8), 839–864. https://doi.org/10.1016/j.jastp.2006.01.008

Sergeev, V. A., Liou, K., Newell, P. T., Ohtani, S. I., Hairston, M. R., & Rich, F. (2004). Auroral streamers: Characteristics of associated precipitation, convection and field-aligned currents. *Annales Geophysicae*, *22*, 537–548. https://doi.org/10.5194/angeo-22-537-2004

Sheng, C., Deng, Y., Wu, Q., Ridley, A., & Häggström, I. (2015). Thermospheric winds around the cusp region. *Journal of Geophysical Research: Space Physics*, *120*(2), 1248–1255. https://doi.org/10.1002/2014ja020028

Shi, Y., Zesta, E., Lyons, L. R., Yang, J., Boudouridis, A., Ge, Y. S., et al. (2012). Two-dimensional ionospheric flow pattern associated with auroral streamers. *Journal of Geophysical Research: Space Physics*, *117*(A2). https://doi.org/10.1029/2011ja017110

Weimer, D. R. (2005). Improved ionospheric electrodynamic models and application to calculating Joule heating rates. *Journal of Geophysical Research: Space Physics*, *110*(A5). https://doi.org/10.1029/2004ja010884